*R*esearch in
*A*stronomy and
*A*strophysics

Group-scale asymmetric abundance structures in the NGC 533 group *

Jun-Hua Gu[1], Hai-Guang Xu[1], Jing-Ying Wang[1], Yu Wang[2], Shao-Feng Xu[1],
Zhen-Zhen Qin[1], Li-Yi Gu[3], Tao An[2], Zhong-Li Zhang[4] and Min Lei[5]

[1] Department of Physics, Shanghai Jiao Tong University, Shanghai 200240, China;
tompkins@sjtu.edu.cn
[2] Shanghai Astronomical Observatory, Shanghai 200030, China
[3] Department of Physics, School of Science, The University of Tokyo 7-3-1 Hongo, Bunkyo-ku,
Tokyo 113–0033, Japan
[4] Max-Planck-Institute of Astrophysics, Karl-Schwarzschild-Str.1, Postfach 1317, 85741
Garching, Munich, Germany
[5] School of Mechanical Engineering, Shanghai Jiao Tong University, Shanghai 200240, China

Abstract By performing a two dimensional spectral analysis on the galaxy group NGC 533 with high-quality *Chandra* data, we find that the metal abundance distribution in this group is anisotropic. In the area around $2.5'$ from the center, we find two concentrations of high abundance structures, in which the abundances are significantly higher than their surrounding regions at the 90% confidence level. We find that the total iron mass in these two regions agrees with the iron mass synthesized in the central dominant galaxy in $0.12^{+0.08}_{-0.03}$ Gyr. The double-sided configuration of the high abundance structure, together with the point-like radio emission in the center suggests that the abundance structures could have been transported from the center to their present positions by active galactic nucleus (AGN) activity. We further calculate the energy required for transport, and find that it could have been supplied during an AGN period. However, considering that this group is reported to have experienced a recent merger, the possibility that this merger is responsible for the abundance structures still cannot be excluded.

Key words: galaxies: clusters: individual (NGC 533) — galaxy: abundances — intergalactic medium — X-rays: galaxies: clusters

1 INTRODUCTION

Metallicity distributions in galaxy groups and clusters indicate events that happened in their evolutionary history. They record the effects of historical processes like mergers, active galactic nucleus (AGN) activity, supernovae, etc. Dozens of galaxy clusters and groups with asymmetric and anisotropic abundance structures have been found, e.g. Abell 1060 (Hayakawa et al. 2004, 2006),

Abell 2199 (Johnstone et al. 2002), AWM7 (Furusho et al. 2003), HCG 62 (Gu et al. 2007), M87 (Simionescu et al. 2008), and the RGH 80 group (Cui et al. 2010). However, at present in some sources, the detailed processes which are responsible for such abundance structures are still not well understood. For example, in HCG 62 the authors reported a huge well-shaped high abundance arc about 30 kpc from the center, whose abundance is about twice that of the surrounding regions. Current observed data indicate that both an AGN and a recent minor merger could be the potential reason, but no firm conclusion has been reached. A well-defined model of the actual mechanism of metal enrichment and the way it spreads through galaxy groups on the scale of clusters relies on the accumulation of many such examples and further improved hydrodynamic simulations in the future.

In this work, we report our studies of the two-dimensional abundance structures in a nearby galaxy group NGC 533 ($z = 0.017385$; Wegner et al. 1999). NGC 533 is a gas-rich, luminous group in X-rays. It is dominated by the cD/E3 galaxy NGC 533. The angular size distance of NGC 533 is calculated to be 61.8 Mpc (Willick et al. 1997) through the $D - \sigma$ relation. In this paper, we use the cosmological constants of $H_0 = 73$ km s^{-1} Mpc^{-1}, $\Omega_m = 0.27$, and $\Omega_\Lambda = 0.73$. We utilize the solar abundance standards of Grevesse and Sauval (1998), where the iron abundance relative to hydrogen is 3.16×10^{-5} in number. Throughout the paper we quote errors at the 68% confidence level unless mentioned otherwise.

2 OBSERVATION AND DATA REDUCTION

The NGC 533 group was observed with *Chandra* on 2002 July 28 (ObsID 2880) for a total exposure of 38.1 ks with CCDs 3, 5, 6, 7, and 8 of the Advanced CCD Imaging Spectrometer (ACIS) in operation. The center of the group-dominating galaxy NGC 533 was positioned close to the nominal aiming point on the back-illuminated S3 chip (CCD 7) with a small offset of $0.9''$. The events were collected with a frame time of 3.2 s and telemetried in the VFaint mode, as the focal plane temperature was set to $-120°$. In this work we use the standard *Chandra* data analysis software package CIAO (version 4.3) and apply the latest package CALDB (version 4.4.3) to process the data extracted from the ACIS-S3 chip. We keep events with *ASCA* grades 0, 2, 3, 4, and 6, and remove all the bad pixels, bad columns, columns adjacent to bad columns and node boundaries. We examine the lightcurves extracted from the source-free regions on the S3 chip and detect no strong occasional background flares. Based on the above processing, we obtain a total of about 9.8×10^4 photons in the level-2 S3 event list.

3 X-RAY, OPTICAL AND RADIO IMAGES

In Figure 1, we show the exposure corrected *Chandra* $0.7 - 7$ keV X-ray image (Fig. 1(a)) that is smoothed with a Gaussian kernel of width $4''$ and the Digitized Sky Survey B-band image (Fig. 1(b)) of the NGC 533 group. We overlay the VLA 1.4 GHz image contour on Figure 1(b). We find that the X-ray peak of the NGC 533 group (R.A.=$01^h25^m31.3^s$, Dec=$01°45'33''$; marked as a "+") is consistent with the position of the central dominant galaxy NGC 533. The X-ray emission of this group appears to be highly symmetric in the whole field of view of CCD 7, and almost no substructure can be recognized by eye. According to Dong et al. (2010), there are two cavities in the central region, however with only visual detection, we can find neither. The radio emission of this group in the 1.4 GHz band possesses a point-like feature that coincides with the X-ray peak and the optical center of the NGC 533 galaxy. This suggests that NGC 533 hosts an AGN.

We fit the azimuthally averaged surface brightness profile with a $\beta-$model

$$S(r) = S_0 \left[1 + \left(\frac{r}{r_{\rm c}} \right)^2 \right]^{-3\beta + 1/2} + S_{\rm bkg}, \tag{1}$$
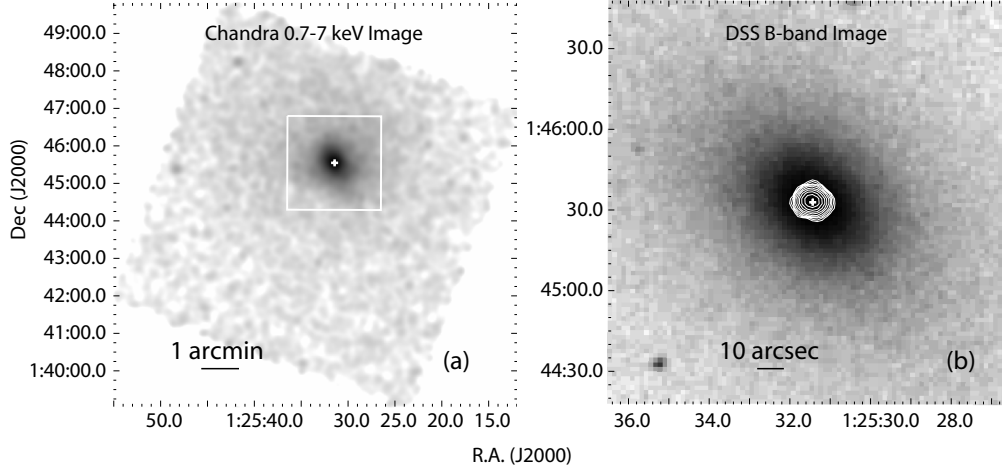
Fig. 1 (a) $0.7 - 7$ keV *Chandra* ACIS-S3 image that has been corrected for exposure and smoothed with a Gaussian kernel of width $4''$. (b) The DSS B-band optical image of NGC 533 is overlaid with the VLA 1.4 GHz radio intensity contours. The field of view of the DSS image is marked as a white box in (a). In both (a) and (b), we mark the X-ray peak with a "+" symbol.

Table 1 Best-fit Parameters of the Azimuthally Averaged Surface Brightness Profile

Parameter	Unit	Value
S_0	cts s^{-1} cm^{-2} pixel^{-2}	$(5.16 \pm 0.53) \times 10^{-7}$
r_c	arcmin	$(9.15 \pm 0.53) \times 10^{-2}$
β	$-$	0.51 ± 0.01
S_{bkg}	cts s^{-1} cm^{-2} pixel^{-2}	$(1.21 \pm 0.15) \times 10^{-9}$
χ^2/dof	$-$	$259.1/137$

where S_0, r_{c}, β, and S_{bkg} are the central surface brightness, core radius, slope, and background, respectively. The best-fit parameters are summarized in Table 1, and the plot of the best-fit model curve is shown in Figure 2(a). We also tried a two $\beta-$ model, but a non-physical result was derived.

To detect whether there is any underlying substructure, we perform a 2-D $\beta-$model fitting to the exposure corrected $0.7 - 7$ keV X-ray image and examine the residuals. The 2-D $\beta-$model is defined as

$$S(\boldsymbol{r}) = S_0 \left[1 + \left(\frac{r}{r_{\mathrm{c}}} \right)^2 \right]^{-3\beta+1/2} + S_{\mathrm{bkg}}, \tag{2}$$

where

$$r = \sqrt{\boldsymbol{r'}^T \boldsymbol{r'}}, \tag{3}$$

$$\boldsymbol{r'} = \begin{bmatrix} x' \\ y' \end{bmatrix} = \begin{bmatrix} \sqrt{\epsilon}\cos\theta & \sqrt{\epsilon}\sin\theta \\ -\frac{1}{\sqrt{\epsilon}}\sin\theta & \frac{1}{\sqrt{\epsilon}}\cos\theta \end{bmatrix} \begin{bmatrix} x - x_0 \\ y - y_0 \end{bmatrix}, \tag{4}$$

(x_0, y_0) is the coordinate of the X-ray peak, θ is the position angle of the major axis of the isophotes, and ϵ is the ratio of the major and minor axes of the isophotes. We calculate the ratio between the residuals and the error of the image

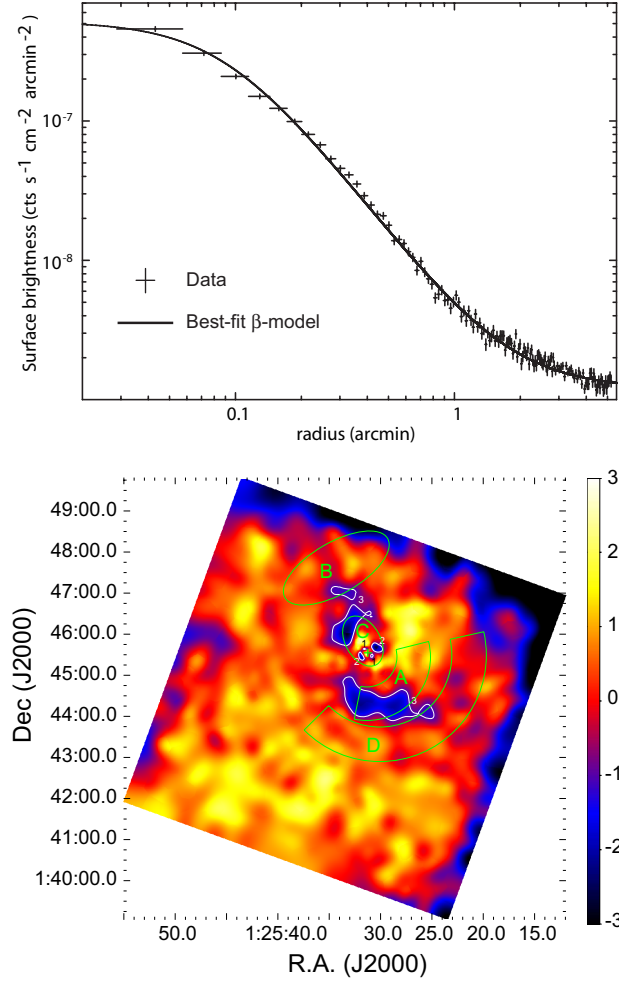$$\Delta = \frac{S_{\mathrm{data}} - S_{\mathrm{model}}}{\sigma}, \tag{5}$$

Fig. 2 *Top*: The $\beta-$model fitting of the azimuthally averaged $0.7-7$ keV surface brightness profile. *Bottom*: The residuals between the $0.7-7$ keV image and the best-fit 2-D $\beta-$model prediction in the unit of image error. We mark the X-ray peak with a "+" symbol. The white contours are the levels of -1, which enclose the regions that are significantly below the $\beta-$model prediction over the 1σ confidence level. The regions A-D are defined in the abundance map shown in Figure 5(b) (see Sect. 5).

as shown in Figure 2(b). We mark the region with $\Delta < -1$ in the central $2.5'$ (44.9 kpc) region with green contours, which means the surface brightness is below the prediction of the $\beta-$model at over a 1σ confidence level. Ignoring the fragments caused by fluctuation, there are three pairs of low surface brightness regions near the center (marked as 1, 2, and 3 according to their distances from the X-ray peak). The first pair of cavities is just what was discovered by Dong et al. (2010).

4 AZIMUTHALLY AVERAGED SPECTRAL ANALYSIS

We performed a deprojected analysis of the *Chandra* spectra extracted from a set of annuli, which span over $0' - 6'$ ($0 - 107.9$ kpc) and are all centered on the X-ray peak. We limited the fittings

to $0.7 - 7$ keV to minimize the effects of the instrumental background at higher energies and the calibration uncertainties at lower energies. We fit the spectra with an absorbed APEC model, and use the XSPEC model PROJCT to evaluate the influence of the outer spherical shells on the inner ones. Since allowing the absorption to vary did not improve the fit, we fixed it to the Galactic value $N_{\rm H} = 3.02 \times 10^{20}{\rm cm}^{-2}$ (Dickey & Lockman 1990). We show the best-fit deprojected gas temperature and metal abundance profile in Figure 3 with $\chi^2/{\rm dof} = 946.3/913 = 1.03$. The best-fit deprojected gas temperature increases steadily from about $\simeq 0.7$ keV at the X-ray peak to $\simeq 1.5$ keV in $> 2'$ (36.0 kpc), suggesting it is the origin of the gas for the group in the outer regions. The abundance profile possesses two off-center peaks at $\simeq 1.7'$ (30.6 kpc) and $\simeq 3.9'$ (70.1 kpc) from the center, respectively.

We note that in the inner $2'$ (36 kpc) region the temperature profile is rather steep, therefore a one-temperature (1T hereafter) model fitting may not be enough. Thus we add another thermal component to the inner three annuli and fit the spectra again. The two thermal components share a common metal abundance. We obtain a $\chi^2/{\rm dof} = 932.9/908 = 1.03$. The best-fit deprojected gas temperature and abundance profiles are shown in Figure 4. From the temperature profile, we find that the high temperatures ($T_{\rm h}$ hereafter) in the inner three annuli are all around 1.5 keV, which are close to the temperatures in the outer five annuli. However, the low temperature ($T_{\rm l}$ hereafter) distribution in the inner three annuli possesses a similar trend as that appearing in the above 1T fitting, which increases steadily from $\simeq 0.7$ keV in the center to $\simeq 1.5$ keV in the outer $> 2'$ (> 36 kpc) regions and converges to the T_h. On the other hand, for the abundance profile, we find that the two off-center abundance peaks still exist, but the position changes slightly. In the 1T fitting, the inner peak occupies the third and forth annuli ($1' - 2.4'$; $18 - 43.2$ kpc), while in the two-temperature (2T) fitting, it occupies the second to forth annuli ($0.4' - 2.4'$; $7.2 - 43.2$ kpc), i.e. it becomes broader and closer to the center. In addition, the outer peak moves from the fifth annulus in the 1T fitting to the sixth annulus in the 2T fitting. The abundances of the two peaks are both higher than in the 1T fitting.

5 2-D SPECTRAL ANALYSIS

Following the method of Gu et al. (2007), we calculate the two dimensional temperature and abundance maps of the X-ray gas and their corresponding 1σ error maps (Fig. 5). The extracted spectrum is fitted with an absorbed APEC model, with the absorption fixed to the Galactic column density $N_{\rm H} = 3.0 \times 10^{20}$ cm^{-2} (Dickey & Lockman 1990), and the redshift fixed to 0.017385. The *Chandra* blank field spectra are used as the background.

We find that the temperature distribution of the NGC 533 group appears to be roughly symmetric, with the temperature slightly higher in the NE direction. The temperature near the X-ray peak is 0.7 keV; it increases to $\simeq 1$ keV at $0.5'$ (9.0 kpc) from the center and $\simeq 1.4$ keV outside $1'$ (18.0 kpc). This feature agrees with other galaxy groups (e.g., HCG 62; Gu et al. 2007).

Despite the symmetry of the temperature, the abundance distribution appears to be anisotropic. There are mainly two bulks of high abundance regions, which are located toward the SW (marked as A) and NE (marked as B) from the center, respectively. The average abundances in regions A and B are 1.8 $Z_\odot$, with a typical error of $\simeq 0.6$ $Z_\odot$, and 2 $Z_\odot$, with a typical error of $\simeq 0.8$ $Z_\odot$, respectively. Also, in the central region (marked as C) and outside region A (marked as D), the abundances are 0.5 $Z_\odot$ and 0.2 $Z_\odot$, respectively, both with typical errors of 0.2 $Z_\odot$. To compare the correlations between the abundance structures and the X-ray image structures, we overlay the contours in Figure 2(b) on the abundance map, and mark the regions A-D in Figure 2(b). We find a correlation between the third pair of cavities and the two high abundance structure regions A and B, i.e. 1) the directions of regions A and B agree with those of the third pair of cavities; 2) the south cavity is just located in region A. Although the north cavity does not exactly match region B, this
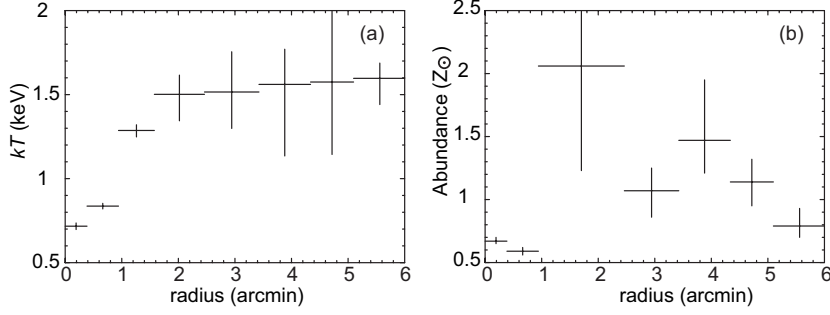
Fig. 3 Deprojected temperature (a) and abundance (b) profiles of the central $\simeq 6'$ (107.9 kpc) region of NGC 533. The error bars are at the 90% confidence level.
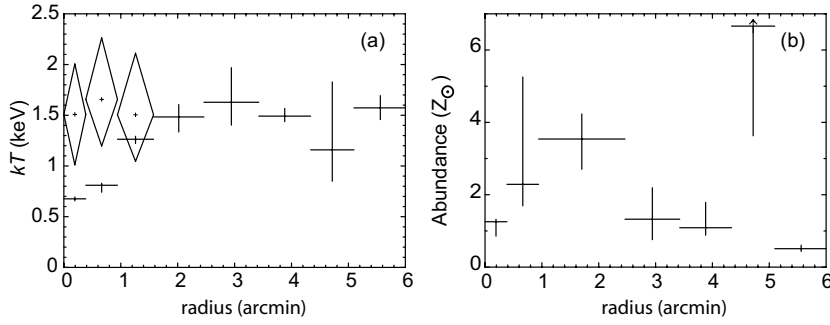

Fig. 4 Deprojected temperature (a) and abundance (b) profiles obtained with the 2T model fitting of the central $\simeq 6'$ (107.9 kpc) region of NGC 533. In the inner three annuli, the data points with diamond error bars are the $T_{\rm h}$ and the data points with cross error bars are the $T_{\rm l}$. The error bars are at the 90% confidence level for the temperature profile. The upper limit of the sixth data point of the abundance profile is not well constrained.

mismatch may be caused by the low signal-to-noise ratio (SNR) and uncertainties of the response near the edge of the CCD.

From the above azimuthally averaged spectral analysis, we have shown that the spectra may posses two thermal components; we can also check under the 2T assumption whether the characteristic abundance structures still exist. Since the 2T model has more free parameters that need to be determined, we re-divide the group into a set of pie-piece shaped regions to increase the SNR in each region. In order to prevent the abundance structures from being smeared by the division, we define the regions to ensure that each high abundance region in Figure 5(b) is contained in a single pie-piece shaped region. We do not consider the outer $> 3'$ (> 54 kpc) regions here because of their low SNR. The model used to fit the spectra is the same as what we used in the 2T model fittings in the above azimuthally averaged spectral analysis, except that the projection effects are not corrected. We present the derived $T_{\rm h}$, $T_{\rm l}$ and the abundance distributions, together with their 68% confidence level lower and upper limits in Figure 6. We find that although the abundances are systematically higher than those derived with the 1T fitting, the two high abundance structures (regions A and B in Fig. 5(b)) still exist. Compared with the abundance map derived with the 1T fitting above, the main difference is that the abundance in the central region (region C in Fig. 5(b)) is no longer significantly
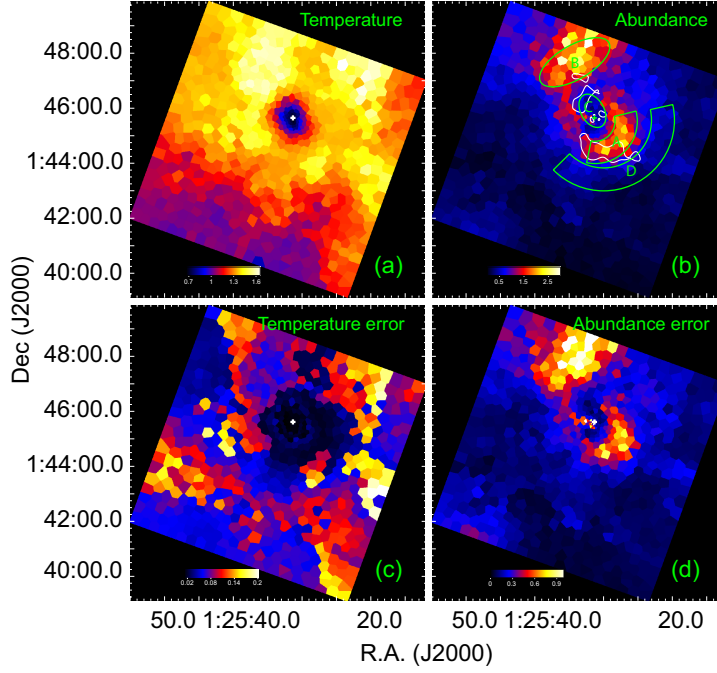
Fig. 5 (a) Temperature map of NGC 533. (b) Abundance map of NGC 533. Regions A, B, C and D are used to extract the spectra to confirm the existence of the featured high abundance structures. We overlay the contours in Figure 2(b), which enclose three pairs of cavities on the abundance map. (c) The 1σ error map for the temperature distribution. (d) The 1σ error map for the abundance distribution. We mark the X-ray peak with a "+" symbol.

lower than in region A. Despite this, the major phenomenon that we discovered in the 1T fitting, i.e. the asymmetric and double-sided distributions of the high abundance regions A and B, is still significant in the 2T fitting.

In order to verify the characteristic abundance structures detected in the abundance maps, we extract the spectra from regions A-D as defined in Figure 5(b) and perform model fittings. The best-fit model parameters are summarized in Table 2. The spectra are first fitted with the 1T model. We find that the spectra extracted from regions B and C cannot be well fitted with a 1T model, so we perform a 2T fit on these two regions, and the fits are significantly improved. We find that the abundance of region B remains high when fitted with the 2T model. For region C, whose abundance was originally lower than regions A and B, its abundance increases significantly in the 2T model fitting.

We plot the fit-statistic contours of gas temperature and abundance obtained with the 1T model fitting at the 68% and 90% confidence levels (Fig. 7) for regions A-D. It is clear that in regions A and B, the abundances are higher than those in the region outside region A and those in the 1T result of the central region at a significance of 90%. Although the central region may need a 2T spectral model to describe it, which may lead to a significantly higher abundance, we still confirm the existence of the two asymmetric and double-sided distributions of high abundance regions A and B.

To obtain information about historical supernova contributions in regions A and B, we perform 1T VAPEC spectral fittings in these two regions. Except for He, Si and Fe, we tie abundances of all other elements to that of C. We fix the He abundance to $1\,Z_{\odot}$, and set Si and Fe as free parameters. In
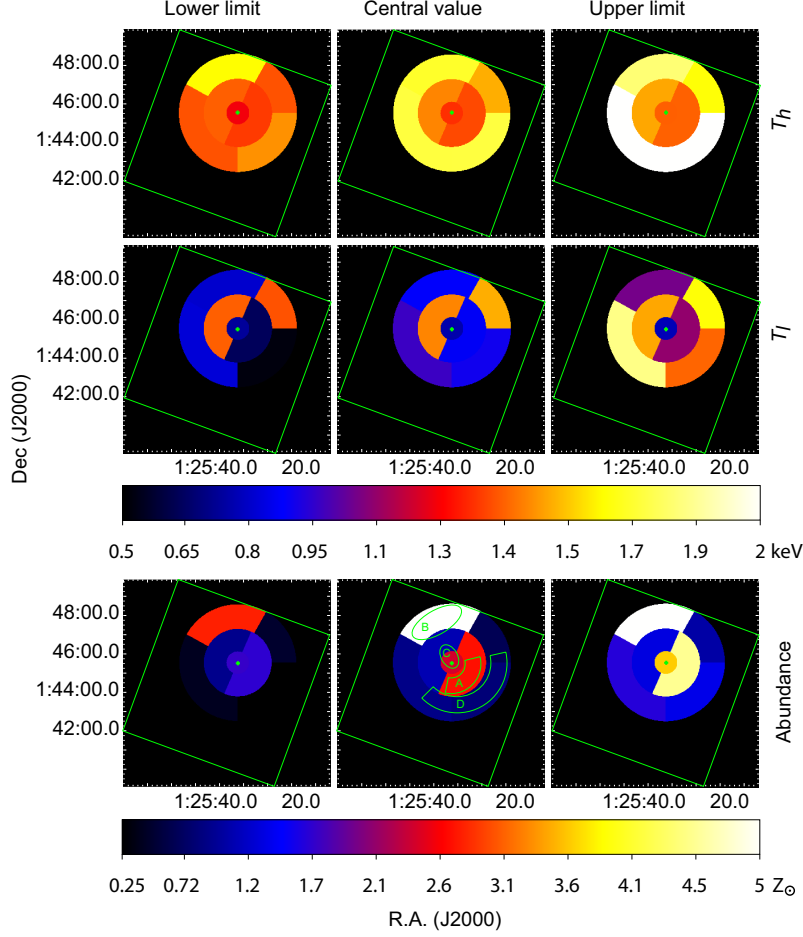
Fig. 6 The temperature and abundance maps of NGC 533, that were derived from pie-piece shaped regions. The three rows from top to bottom are T_h, T_l and abundance, respectively. The three columns from left to right are the lower limit, central value and upper limit of the corresponding quantities, respectively. The field of views of these maps are the same as those of Figure 5, while the green squares represent the region of the *Chandra* ACIS-S CCD. We mark the X-ray peak with a "+" symbol.

region A, the Fe and Si abundances are $1.31^{+0.41}_{-0.47} Z_\odot$ and $0.93^{+0.34}_{-0.29} Z_\odot$, respectively, with $\chi^2/\mathrm{dof} = 0.99$. In region B, the Fe and Si abundances are $1.2^{+0.49}_{-0.22} Z_\odot$ and $1.43^{+0.89}_{-0.53} Z_\odot$, respectively, with $\chi^2/\mathrm{dof} = 1.23$. The temperatures are both in agreement with those obtained with the 1T fittings within the error range.
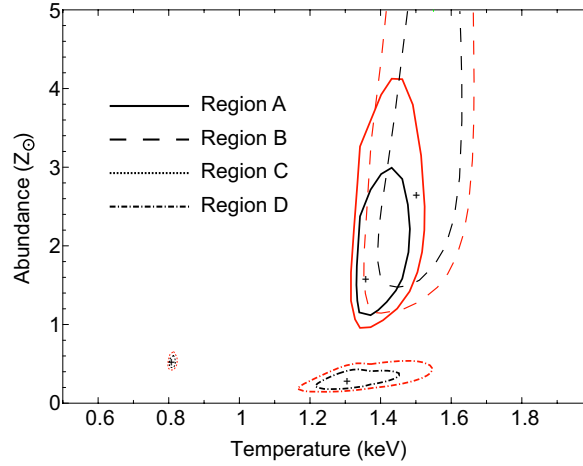
6 ELECTRON DENSITY PROFILE

We obtain the electron density profile using the X-ray surface brightness profile $S(r)$ and cooling function Λ distribution, which is a function of gas temperature T and the metal abundance A. We

Table 2 Best-fit Spectral Models for the Four Regions Defined in Fig. 5(b)[†]

Region No.	Temperature (keV)	Abundance ($Z_\odot$)	χ^2/dof
	WABS×APEC		
A	$1.36^{+0.13}_{-0.04}$	$1.56^{+1.32}_{-0.51}$	77.2/80
B	$1.52^{+0.11}_{-0.13}$	$2.62^{+0.47}_{-1.18}$	102.6/81
C	0.81 ± 0.01	$0.54^{+0.13}_{-0.09}$	147.9/113
D	$1.30^{+0.17}_{-0.10}$	$0.25^{+0.17}_{-0.09}$	98.6/107
	WABS×(APEC+APEC)		
B	$1.66^{+0.25}_{-1.0}/0.86^{+0.45}_{-0.24}$	$4.1^{+0.9}_{-2.3}$	98.6/79
C	$1.31^{+0.19}_{-0.14}/0.74^{+0.03}_{-0.05}$	$2.30^{+2.68}_{-0.96}$	125.2/111

Notes: [†] We fit the spectra with an absorbed APEC (for regions A-D) or an absorbed APEC+APEC (for regions B & C) model with the absorption and redshift fixed to the Galactic value ($N_H = 3.02 \times 10^{20}$ cm^{-2}; Dickey & Lockman 1990) and $z = 0.017385$. The confidence levels here are all 90%.

Fig. 7 Two-dimensional fit-statistic contours of temperature and abundance at the 68% and 90% confidence levels for the four regions defined in Figure 5(b).

assume the electron density profile follows the two$-\beta$ model

$$n_e(R) = n_{0,1}\left[1 + \left(\frac{R}{R_{c,1}}\right)^2\right]^{-3\beta_1/2} + n_{0,2}\left[1 + \left(\frac{R}{R_{c,2}}\right)^2\right]^{-3\beta_2/2}, \tag{6}$$

where for each component n_0, R_c, and β represent the central electron density, core radius, and the slope, respectively. The corresponding X-ray surface brightness is then calculated as

$$S(r) = \int_r^\infty \Lambda(T, A)n_e^2(R)\frac{RdR}{\sqrt{R^2 - r^2}} + S_{\text{bkg}}, \tag{7}$$

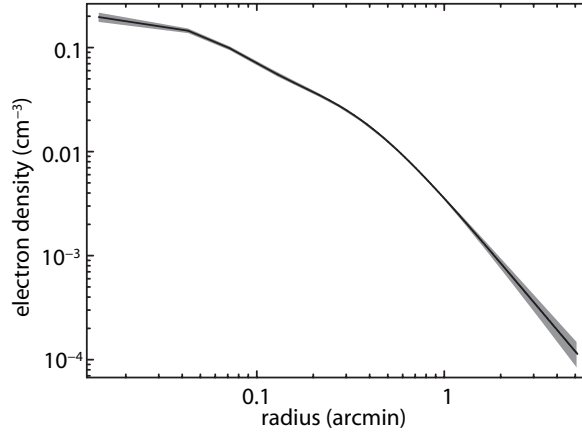**Fig. 8** Best-fit electron density profile and its 68% confidence level error boundary.

where S_{bkg} is a free parameter representing the diffuse X-ray background. Equation (7) is used to fit the measured surface brightness to derive the electron density $n_{\mathrm{e}}(R)$. We show the best-fit electron density profile in Figure 8.

7 DISCUSSION

Through the 1T analysis above, we identify a pair of high abundance regions toward the SW (region A) and NE (region B) of the X-ray peak of NGC 533, in which the abundance is significantly higher than their surrounding regions at the 90% confidence level. The SW high abundance structure forms an arc with a radius of $1.1'$ (19.8 kpc) and a thickness of about $0.82'$ (14.7 kpc). In addition, the NE high abundance region approximately forms an ellipse with semi-major and semi-minor axes of $0.62'$ (11.1 kpc) and $1.4'$ (25.2 kpc), respectively. In our 2T analysis, the above results are confirmed, except that the abundance of the central region is no longer significantly lower than regions A and B. From the 2T abundance map divided into pie-piece shaped regions, we can still recognize the high abundance regions A and B, which means that the asymmetrically distributed abundance structures can be detected under both 1T and 2T assumptions.

Here we calculate the iron mass contained in regions A and B. The abundance obtained under the 1T assumption is used here as a lower limit, since the 2T results are significantly higher. We assume the 3D geometry of region A to be a partial spherical shell with inner and outer radii of $0.69'$ (12.4 kpc) and $1.51'$ (27.1 kpc), respectively, and with a cone angle of $116°$. The 3D geometry of region B is assumed to be a prolate spheroid, with its semi-major and semi-minor axes of $1.44'$ (25.9 kpc) and $0.62'$ (11.2 kpc), respectively, and the distance from its center to the X-ray peak is $2.2'$ (39.5 kpc). Based on the abundance obtained from the 1T analysis and electron density obtained above, we calculate the total iron mass contained in regions A and B to be $3.68^{+3.11}_{-1.20} \times 10^6\ M_\odot$ and $1.22^{+0.22}_{-0.55} \times 10^6\ M_\odot$, respectively.

By using the method described in Wang et al. (2005), we calculate the time needed to produce iron with the same total mass of iron that is contained in regions A and B to be $0.12^{+0.08}_{-0.03}$ Gyr, according to the B-band optical luminosity $L_B = 12.4 \times 10^{10}\ L_\odot$ of the central dominant galaxy NGC 533 taken from Leda (Paturel et al. 2003). Note that we utilize the abundance obtained from the 1T fitting. However, even if we use the abundance from the 2T fitting, the enrichment time will not be increased by twice and is still significantly shorter than the age of the universe. This demonstrates that the high abundance regions A and B can be produced in the central dominant galaxy NGC 533 and transported to their current position.

Following the method shown in Wang et al. (2005), we calculate the SN Ia contribution to the iron mass in regions A and B by measuring the abundance ratio Si/Fe. According to our measurement of the Fe and Si abundance in Section 5, we derive SN Ia contributions of $86.8^{+10.8}_{-23.7}\%$ and $66.0^{+23.0}_{-28.8}\%$ in regions A and B, respectively. These values are consistent with those in other galaxy clusters and groups (e.g., Wang et al. 2005; Ishimaru & Arimoto 1997).

Since we have found a point-like radio structure in the center of the dominant galaxy NGC 533, it is natural that these two high abundance structures could have been formed by the AGN activity in NGC 533. Other evidences that support the AGN origin of the high abundance structures are 1) in Section 3, we have proved that the surface brightness in the NE and SW directions is significantly lower than the 2D $\beta-$model prediction, which implies that there are corresponding AGN cavities in the directions of the high abundance structures; and 2) the high abundance regions A and B are distributed over the two sides (i.e. NE and SW) of the X-ray peak, which agrees with the activity paradigm of AGNs that usually produces double-sided jets.

The most likely mechanism where an AGN transfers metal from the center to the peripheral regions is that the AGN activity could produce rising bubbles, which contain metal enriched gas. In this scenario, we calculate the energy required to drive such kind of transportation. Since the bubbles are produced in the center of the group and rise to their present positions, we should deduce their initial state according to their final (i.e. present) state. We denote the initial pressure to be p_i, present pressure to be p_f, and present volume to be V_f, and assume that they expand in a polytropic process with a polytropic index of N. The initial volume can be calculated as

$$V_\mathrm{i} = \left(\frac{p_\mathrm{f}}{p_\mathrm{i}}\right)^{1/N} V_\mathrm{f}. \qquad (8)$$

So the energy required to produce the bubble with a volume V_i in an environment with pressure p_i is

$$H = E + pV \ = \frac{\gamma}{\gamma - 1}\, p_\mathrm{i} V_\mathrm{i} \ = \frac{\gamma}{\gamma - 1}\, p_\mathrm{i} \left(\frac{p_\mathrm{f}}{p_\mathrm{i}}\right)^{1/N} V_\mathrm{f}, \qquad (9)$$

where E is the gas' internal energy, $\gamma = 4/3$ is the adiabatic index of the relativistic gas, $p = nkT$, and n is the gas' particle density. According to the 3D geometry assumption we utilized above, we calculate the total energy required to produce the bubbles in regions A and B to be $1.634 \times 10^{58} - 8 \times 10^{58}$ erg corresponding to the range of N from 1 (isothermal process) to $4/3$ (adiabatic process). This amount of energy can be produced in one AGN activity period in some cases of clusters and groups (e.g., Wise et al. 2007). Similar AGN-driven metal transportation has been observed in other sources. For example in galaxy cluster M87, Simionescu et al. (2008) found enhancement of Fe abundance in the two X-ray bright arm regions. The metal abundance in the cool gas in the arm regions was measured to be $\sim 2.2\ Z_\odot$, which is similar to the abundance in regions A and B in this work. The authors interpreted it as the result of metal enrichment by a rising plasma bubble produced by the AGN activity. Considering that we find a connection between the high abundance structures and the X-ray bubbles, the results in M87 by Simionescu et al. (2008) support our speculation that the metal transport in NGC 533 is also driven by rising bubbles produced by an AGN.

Although the above calculations show that the energy required to transfer the metal enriched gas from the center to its present position agrees with what AGN activity can supply, we still cannot exclude the possibility that a recent merger drove the transfer. By studying the line of sight velocity distribution, Finoguenov et al. (2007) suggest that the NGC 533 group recently experienced a merger. However, how the merger process created the double-sided high abundance structure requires a further confirmation by numerical simulations.

8 SUMMARY

Through the 2-D spectral analysis on the high-quality *Chandra* data of the NGC 533 group, we found a pair of high abundance regions that are distributed nearly symmetrically with respect to the X-ray peak. We find that the total iron mass contained in these two regions can be synthesized by NGC 533 within $0.12^{+0.08}_{-0.03}$ Gyr, and the energy required to transfer the gas in these two regions from the group center to the present positions agrees with what can be produced by an AGN. So an AGN can be the potential mechanism to form these two high abundance regions. However, we still cannot exclude the possibility of a recent merger.

References

Cui, H.-J., Xu, H.-G., Gu, J.-H., et al. 2010, RAA (Research in Astronomy and Astrophysics), 10, 301
Dickey, J. M., & Lockman, F. J. 1990, ARA&A, 28, 215
Dong, R., Rasmussen, J., & Mulchaey, J. S. 2010, ApJ, 712, 883
Finoguenov, A., Ponman, T. J., Osmond, J. P. F., & Zimer, M. 2007, MNRAS, 374, 737
Furusho, T., Yamasaki, N. Y., & Ohashi, T. 2003, ApJ, 596, 181
Gu, J., Xu, H., Gu, L., et al. 2007, ApJ, 659, 275
Hayakawa, A., Furusho, T., Yamasaki, N. Y., Ishida, M., & Ohashi, T. 2004, PASJ, 56, 743
Hayakawa, A., Hoshino, A., Ishida, M., et al. 2006, PASJ, 58, 695
Ishimaru, Y., & Arimoto, N. 1997, PASJ, 49, 1
Johnstone, R. M., Allen, S. W., Fabian, A. C., & Sanders, J. S. 2002, MNRAS, 336, 299
Paturel, G., Petit, C., Prugniel, P., et al. 2003, A&A, 412, 45
Simionescu, A., Werner, N., Finoguenov, A., Böhringer, H., & Brüggen, M. 2008, A&A, 482, 97
Wang, Y., Xu, H., Zhang, Z., et al. 2005, ApJ, 631, 197
Wegner, G., Colless, M., Saglia, R. P., et al. 1999, MNRAS, 305, 259
Willick, J. A., Courteau, S., Faber, S. M., et al. 1997, ApJS, 109, 333
Wise, M. W., McNamara, B. R., Nulsen, P. E. J., Houck, J. C., & David, L. P. 2007, ApJ, 659, 1153